

Compensated thermal conductivity of metallically conductive Ta-doped TiO₂

Joonki Suh, Tarapada Sarkar, Hwan Sung Choe, Joonsuk Park, T. Venkatesan, and Junqiao Wu

Citation: *Appl. Phys. Lett.* **113**, 022103 (2018); doi: 10.1063/1.5044563

View online: <https://doi.org/10.1063/1.5044563>

View Table of Contents: <http://aip.scitation.org/toc/apl/113/2>

Published by the [American Institute of Physics](#)

Articles you may be interested in

[Electrical properties of extended defects in strain relaxed GeSn](#)
Applied Physics Letters **113**, 022102 (2018); 10.1063/1.5034573

[Engineering magnetic heterostructures to obtain large spin Hall efficiency for spin-orbit torque devices](#)
Applied Physics Letters **113**, 022402 (2018); 10.1063/1.5036836

[Exploration of exciton behavior in atomically thin WS₂ layers by ionic gating](#)
Applied Physics Letters **113**, 013104 (2018); 10.1063/1.5022327

[Contributions of the lead-bromine weighted bands to the occupied density of states of the hybrid tri-bromide perovskites](#)
Applied Physics Letters **113**, 022101 (2018); 10.1063/1.5024527

[Terahertz magnon and crystal-field transition manipulated by R³⁺-Fe³⁺ interaction in Sm_{0.5}Pr_{0.5}FeO₃](#)
Applied Physics Letters **113**, 022401 (2018); 10.1063/1.5037119

[Thickness dependence of superconductivity in single-crystal Ta₄Pd₃Te₁₆ nanoribbons](#)
Applied Physics Letters **113**, 022603 (2018); 10.1063/1.5040046

Quantum Design Brings You the Next Generation Magneto-Optic Cryostat



Only be limited by your imagination...

Learn More

Quantum Design
qdusa.com/opticool5

8 Optical Access Ports: 7 Side, 1 Top
Temperature Range: 1.7 K to 350 K
7 T Split-Coil Conical Magnet
Low Vibration: <10 nm peak-to-peak
89 mm x 84 mm Sample Volume
Automated Temperature & Magnet Control
Cryogen Free

Compensated thermal conductivity of metallically conductive Ta-doped TiO₂

Joonki Suh,^{1,a),b)} Tarapada Sarkar,^{2,3} Hwan Sung Choe,¹ Joonsuk Park,⁴
 T. Venkatesan,^{2,3,5,6,7} and Junqiao Wu^{1,8,b)}

¹Department of Materials Science and Engineering, and Tsinghua-Berkeley Shenzhen Institute, University of California, Berkeley, California 94720, USA

²Department of Physics, National University of Singapore, Singapore 117542

³NUSNNI-NanoCore, National University of Singapore, Singapore 117576

⁴Department of Materials Science and Engineering, Stanford University, Stanford, California 94305, USA

⁵Department of Electrical Engineering, National University of Singapore, Singapore 117583

⁶Department of Integrative Science and Engineering, National University of Singapore, Singapore, 117456

⁷Department of Materials Science and Engineering, National University of Singapore, Singapore 117575

⁸Materials Sciences Division, Lawrence Berkeley National Laboratory, Berkeley, California 94720, USA

(Received 14 June 2018; accepted 25 June 2018; published online 10 July 2018)

Electrical and thermal conductivities of epitaxial, high-quality Ta-doped TiO₂ (Ta:TiO₂) thin films were experimentally investigated in the temperature range of 35–375 K. Structurally identified as the anatase phase, degenerate Ta doping leads to high electrical conductivity in TiO₂, reaching $>10^5$ (Ω·m)⁻¹ at 5 at. % of Ta, making it a potential candidate for indium-free transparent conducting oxides. In stark contrast, Ta doping suppresses the thermal conductivity of TiO₂ via strong phonon-impurity scattering imposed by the Ta dopant which has a high mass contrast with Ti that it substitutes. For instance, the near-peak value shows a $>50\%$ reduction, from 9.0 down to 4.4 W/m·K, at just 2 at. % doping at 100 K. Interestingly, further Ta doping beyond 2 at. % no longer reduces the measured total thermal conductivity, which is attributed to a high electronic contribution to thermal conduction that compensates the alloy-scattering loss, as well as possibly the renormalization of phonon dispersion relation in the heavy doping regime originating from doping-induced lattice stiffening. As a result, at high Ta doping, TiO₂ exhibits high electrical conductivity without much degradation of thermal conductivity. For example, near room temperature, 5 at. % Ta doped TiO₂ shows over 3 orders of magnitude enhancement in electrical conductivity from undoped TiO₂, but with only less than 10% reduction in thermal conductivity. The metallic Ta:TiO₂ maintaining reasonable good thermal conductivity might find application in energy devices where good conduction to both charge and heat is needed. *Published by AIP Publishing.*

<https://doi.org/10.1063/1.5044563>

Anatase titanium dioxide (TiO₂) is among the most investigated oxide semiconductors owing to a wide variety of potential applications.^{1,2} It plays vital roles for light energy conversion and harvesting devices by serving as the photocatalyst and transparent conducting oxide (TCO) layer. The relevant physical-chemical properties of TiO₂ are largely dependent on the types and density of point defects incorporated, including extrinsic dopants and native imperfections. For instance, surface point defects such as oxygen vacancies are reportedly known to promote photocatalytic activities^{3,4} and formation of two-dimensional electron gas.⁵ In addition, degenerate doping is of necessity to meet the key requirement of high electrical conductivity for TCO application⁶ and to boost the electrochemical activities for multivalent Mg²⁺ and Al³⁺ ions by generating charge-compensating defects.⁷ In contrast with the well-established relationship between doping and electrical transport of most semiconductors, its effect on thermal transport, particularly in the degenerate regime, remains much less explored. On the other hand, a fundamental understanding of thermal

properties and its relationship with charge transport need to be explicitly developed, given various potential uses of TiO₂, because in many cases designing an efficient heat dissipation route from the active device layer is becoming critically important.

While Nb doping has been most commonly employed,^{8,9} tantalum (Ta) attracts great attention as an alternative dopant for TiO₂. The recent interest in Ta doping stems from a higher solubility exceeding 4×10^{21} cm⁻³ owing to a lower defect formation energy of charged Ta compared to that of Nb,^{10–12} resulting in superior electrical and optical properties with a wider tunability.¹³ Degenerate Ta doping has been shown to induce high electrical conductivity and preserve high transmittances in the visible regime¹⁴ and also realize the coexistence of ferromagnetism and Kondo scattering in this highly correlated electronic system in TiO₂.¹⁵ Herein, we report the concomitant electrical and thermal transport measurements in Ta-doped anatase TiO₂ thin films (Ta:TiO₂). The highest Ta doping reaches up to 5 at. %, which denotes the cation atomic ratio between Ta and Ti. While Ta dopants lead to metallic electrical conduction, they suppress thermal conductivity via strong impurity-phonon scattering. Thermal conductivity gradually decreases upon Ta substitution over a wide temperature range of 35–375 K, but stops decreasing (or even slightly increases in some temperature ranges) at high Ta doping

^{a)}Present address: Department of Chemistry, University of Chicago, Chicago, Illinois 60637, USA.

^{b)}Authors to whom correspondence should be addressed: joonki@uchicago.edu and wuj@berkeley.edu

concentrations. It is found that the electronic thermal conduction cannot explain the observation, and the unexpectedly enhanced sound velocity by compressive-strain-mediated phonon stiffening around Ta dopants might be responsible for such a non-monotonic trend.

We have deposited pristine TiO_2 and Ta: TiO_2 thin films with a thickness of ~ 200 nm using pulsed laser deposition (PLD). For the Ta: TiO_2 , Ta doping concentrations of 0.3, 2, and 5 at. % were prepared. These films were deposited on Si substrates pre-covered with a thin 28 nm SrTiO_3 (STO) at 750°C in an oxygen pressure of 1×10^{-3} . Epitaxial STO (001) thin films were grown as template layers on Si (001) wafers by molecular beam epitaxy (see [supplementary material](#) for details). X-ray diffraction (XRD) spectra were collected using Mo $K\alpha$ excitation. Raman spectra were collected using a 488 nm laser as the excitation source (Renishaw inVia). Cross-sectional transmission electron microscopy (TEM) specimens were prepared using a focus ion beam (FIB, FEI Helios 600i) lift-out technique. Pt layer was first deposited to protect the sample surface, and the sample was subsequently thinned to ~ 100 nm with a Ga ion beam at 30 kV. Cross-sectional imaging was performed using an aberration-corrected TEM (FEI Titan environmental TEM 80–300) with 300 kV electron beam.

Figure 1(b) shows a representative θ - 2θ XRD scan of TiO_2 film prepared on the STO/Si substrate. The deposited films are identified to have a textured tetragonal anatase crystal structure with (001) orientation regardless of the Ta doping density [Fig. 1(a)]. No other crystal phase such as rutile

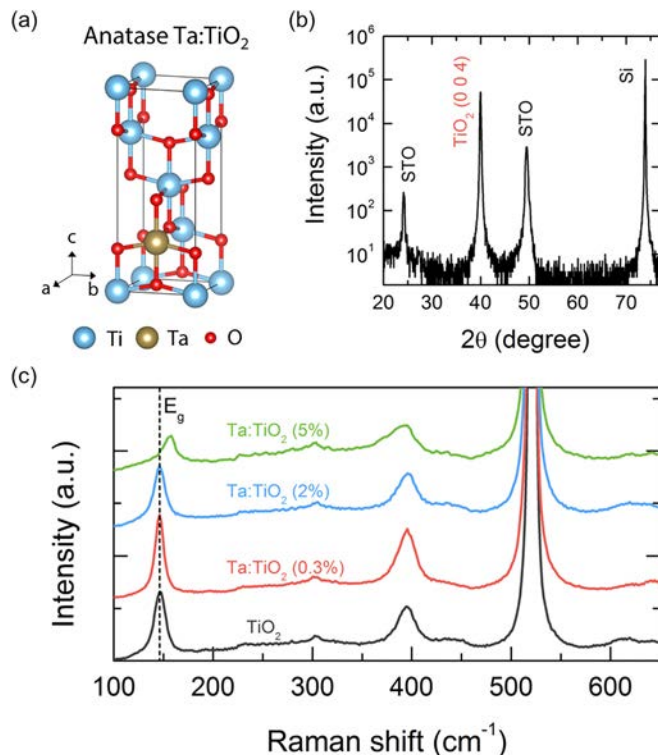


FIG. 1. (a) Crystal structure of anatase TiO_2 substitutionally doped (alloyed) with Ta, in which the [001] axis is vertical. (b) X-ray diffraction pattern of anatase TiO_2 thin film deposited on Si substrate with a buffer layer of SrTiO_3 (STO), taken using the Mo $K\alpha$ radiation. (c) Comparison of Raman spectra of undoped TiO_2 and a series of Ta: TiO_2 (0.3, 2, and 5 at. %) thin films normalized by the Si substrate peak at ~ 520 cm^{-1} .

TiO_2 or Ta_2O_5 are detected in all the films, confirming that the Ta ions are completely dissolved in the anatase TiO_2 within the doping concentrations we employed.¹⁶ Thus, the existence of the STO buffer layer preserves high crystallinity of the grown TiO_2 films, and Si substrate enables us to measure the thermal conductivity (κ) of TiO_2 , thanks to its comparably high κ . The lattice structure of our films was further confirmed by Raman spectroscopy. Raman spectrum [Fig. 1(c)] measured on pristine TiO_2 and Ta: TiO_2 show three Raman peaks at approximately 146, 395, and 630 cm^{-1} , corresponding, respectively, to the lattice vibration modes E_g , B_{1g} , and E_g of anatase TiO_2 with tetragonal symmetry.³ Another commonly observed A_{1g} mode at 515 cm^{-1} is indistinguishable in our case due to overlap with a strong Si Raman peak at 520 cm^{-1} . We also notice an abrupt and pronounced stiffening of the main peak, E_g mode [the dashed line in Fig. 1(c)], in our highest doping case of 5 at. %, suggesting possible phonon renormalization. This will be further analyzed in the following discussion for thermal conductivity measurements. Therefore, it can be concluded that Ta doping does not introduce any heterogeneous crystalline phase, retaining the anatase phase for all samples since subsequent device fabrication and characterization were conducted far below the reported phase transformation temperatures of 500 – 700°C from anatase into rutile.¹⁷

Temperature-dependent electrical conductivity (σ) of the Ta: TiO_2 films with 0.3, 2, and 5 at. % is shown in Fig. 2. They were taken in the four-probe geometry in a Quantum Design physical property measurement system over the temperature range of 5 – 300 K. Owing to the successful incorporation of Ta, a single donor for Ti, the acquired transport data indicates that the doped films are highly degenerate n -type semiconductors, consistent with previous reports.^{14,16} When the doping fraction is ≥ 2 at. %, their temperature dependence exhibits the typical metallic behavior with a definite negative $d\sigma/dT$ down to < 50 K. The highest electrical conductivity reaches $\sim 2 \times 10^5$ ($\Omega\text{-m}$)⁻¹ for the Ta: TiO_2 film with 5 at. % below 50 K. On the other hand, we note that the anatase TiO_2 film without Ta doping remains highly insulating as expected at low temperatures.

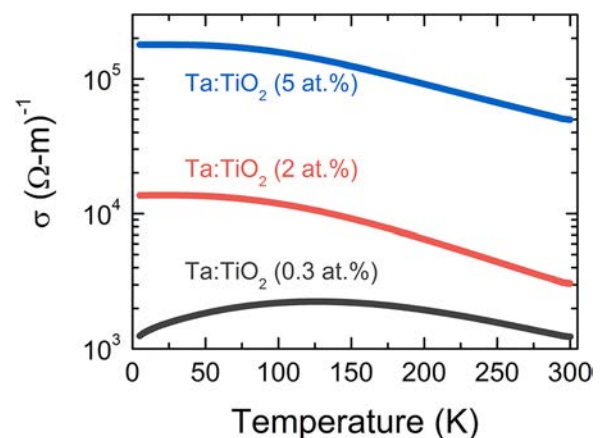


FIG. 2. Temperature dependent electrical conductivity (σ) of the Ta: TiO_2 thin films with different Ta doping concentrations. It was measured in the linear four probe geometry. We note that the undoped anatase TiO_2 film remains electrically very insulating below the detection limit of conductivity.

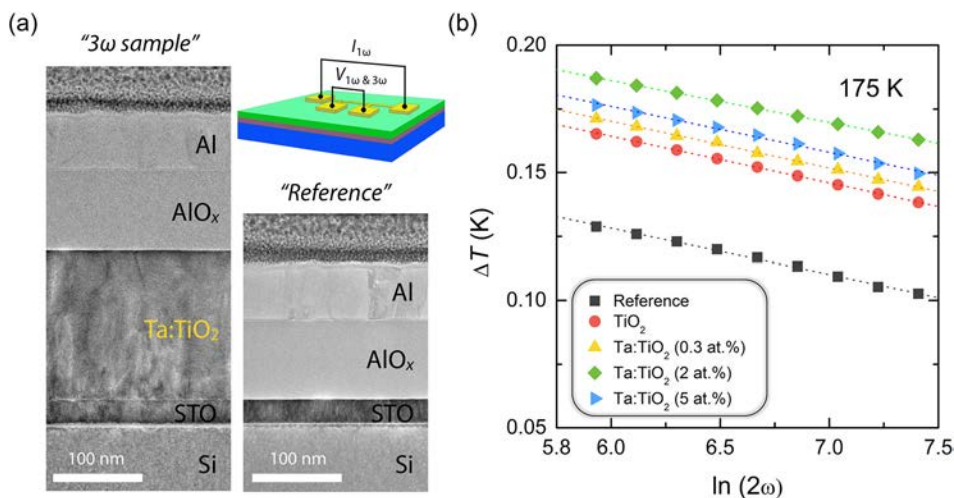


FIG. 3. (a) Cross-sectional TEM images of the fabricated devices for the differential 3ω measurement. The “Reference” specimen was simultaneously prepared, and the only difference is the additional TiO_2 or Ta:TiO_2 film in the “ 3ω sample.” Four-probe Al line heater (yellow) was defined on the top of the ALD-grown AlO_x dielectric layer (green) as shown in the schematic drawing. (b) Measured amplitude of the temperature oscillation, ΔT , of in-phase components as a function of heating frequency, 2ω (in Hz). Representative data displayed here was acquired at 175 K for five different samples including the “Reference” device.

Cross-plane thermal conductivity of undoped TiO_2 and Ta:TiO_2 thin films were measured using the differential 3ω method.¹⁸ For this purpose, two different sample configurations were employed, namely, “ 3ω sample” (with TiO_2 or Ta:TiO_2 layer) and “Reference” (bare substrate without the TiO_2 layer). Using atomic layer deposition (ALD), a 100 nm AlO_x layer was simultaneously deposited on both types of specimen primarily for secure electrical isolation of the metallic conducting Ta:TiO_2 . Four-probe Al line heaters were then patterned on the top of the ALD-grown AlO_x layer using conventional photolithography, as shown in the inset of Fig. 3(a). 3ω measurements were performed in high vacuum ($<10^{-6}$ Torr), and the global temperature was controlled by an external electrical heater and a cryogenic cooler both connected to the sample holder. Direct comparison of cross-sectional TEM images taken from the fabricated “ 3ω sample” and “Reference” devices are presented in Fig. 3(a). Interfaces are completely clean in both samples, and no reaction layers or voids were observed at the interface from the high- and low-resolution TEM characterization.

Figure 3(b) shows the amplitude of the measured in-phase temperature oscillation (ΔT) in the undoped TiO_2 and

Ta:TiO_2 samples along with the reference substrate at 175 K, plotted as a function of the logarithm of heating frequency, 2ω . It was calculated using $\Delta T = 2(dT/dR)(R/V_{1\omega})V_{3\omega}$, where R , $V_{1\omega}$, and $V_{3\omega}$ are the electrical resistance, 1ω voltage, and 3ω voltage of the Al heater, respectively, supplemented with the corresponding temperature coefficient of resistance, dT/dR , which were separately measured afterwards. Based on a linear dependence between the in-phase ΔT and $\ln(2\omega)$, the thermal conductivity of the silicon substrate is estimated to be 230.8 W/m-K at 175 K. It agrees well with earlier reports of bulk Si,¹⁹ thus validates our measurements. In addition, the one-dimensional heat flow generated from a wide heater ($w = 30 \mu\text{m}$) allows determining the average temperature drop solely across the film of our interest by simply subtracting that of the “Reference” specimen. Cross-plane thermal conductivities of the thin films were then calculated as $\kappa = (P/\Delta T)(d/wL)$, where P is the amplitude of the heater power, d is the thickness of film, and L and w are the length and width of the Al heater, respectively.

The measured thermal conductivity as a function of temperature from 35 K to 375 K is presented in Fig. 4(a). The thermal conductivity data of our PLD-grown TiO_2 thin films

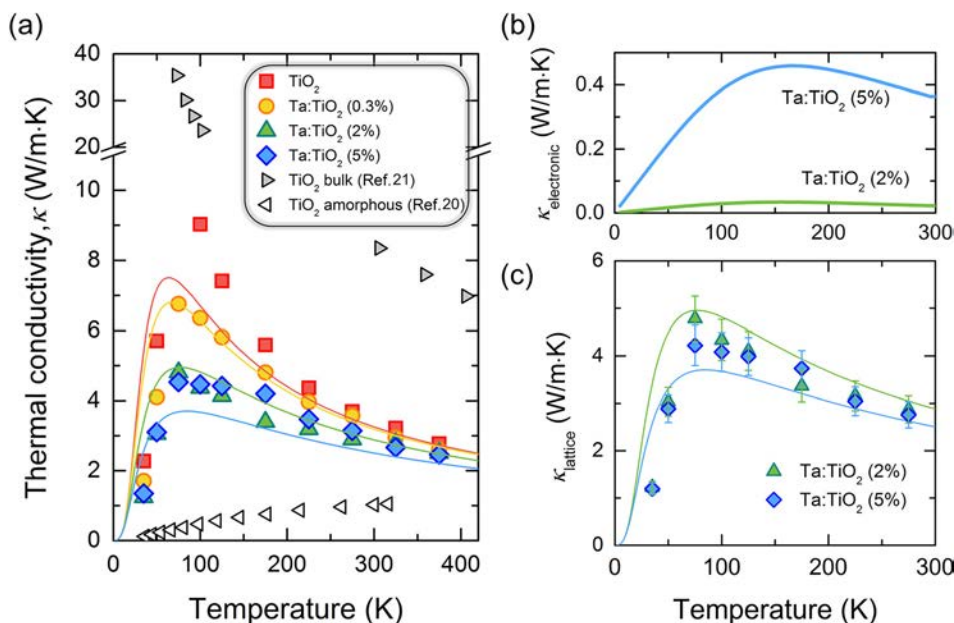


FIG. 4. (a) The measured cross-plane thermal conductivities (κ) of TiO_2 and Ta:TiO_2 thin films as a function of temperature along with the reference values of the bulk and amorphous TiO_2 . The estimated (b) electronic and (c) lattice thermal conductivities of heavily doped Ta:TiO_2 films on the basis of the Wiedemann-Franz law. In both (a) and (c), the lines are the theoretically calculated lattice thermal conductivity for the corresponding Ta doping fractions using the Klemens model.

span a range between the lower and upper bounds previously reported for amorphous thin film²⁰ and bulk crystal,²¹ respectively, all along the cross-plane direction. Ta doping reduces κ of TiO₂ and the magnitude of reduction is dependent on doping concentrations, implying that impurity scattering is critical to thermal transport in the Ta:TiO₂. For instance, the near-peak value shows a twofold decrease from 9.0 down to 4.4 W/m-K around 100 K when the doping approaches 2 at. %. (We note that the real peak value of pristine TiO₂ was not accurately determined in this work due to a negligible ΔT difference of TiO₂ compared to the “Reference” device, presumably due to high thermal conductance through the film at this temperature.)

The effective thermal conductivity from the lattice can be expressed as $\kappa = \int_0^\infty \frac{1}{3} C_v \nu \Lambda_{\text{eff}} d\omega$, where C_v is the volumetric specific heat capacity per unit frequency, ν is the group velocity, Λ_{eff} is the effective mean free path (MFP), and ω is the phonon frequency. In this work, the Born-von Karman-Slack model²² was used to do the calculation in which the phonon dispersion relation is acquired using the known lattice constants and sound velocities. For the latter, all the three acoustic branches are averaged into a single band, with the averaged sound velocity of $\nu = 4140$ m/s from the first principle calculations.²³ Next, Λ_{eff} is calculated using Matthiessen’s rule combining all possible scattering mechanisms: Umklapp (Λ_U), boundary (Λ_B), and impurity scattering (Λ_{imp}) by $\Lambda_{\text{eff}}^{-1} = \Lambda_U^{-1} + \Lambda_B^{-1} + \Lambda_{\text{imp}}^{-1}$. Herein, we used the empirical expressions to describe the different scattering mechanisms separately. First, the Umklapp scattering can be expressed as $\Lambda_U^{-1}(\omega, T) = B_1 \omega^2 T \exp(-\theta/3T)$, where θ is the Debye temperature of the acoustic phonons and T is the absolute temperature. An analytical expression for B_1 ²⁴ is utilized in which $B_1 = \hbar \gamma^2 / M \nu^2 \theta$, where \hbar is the reduced Planck constant, γ is the Grüneisen parameter, and M is the mass of the average atom. For TiO₂, we find the Grüneisen number $\gamma = 2.43$ from pressure dependent Raman measurement,²⁵ and the Debye temperature of all the acoustic branch is $\theta = 466.6$ K.²⁶ Consequently, we calculated the parameter $B_1 = 1.75 \times 10^{-18}$ s/K, and confirmed a reasonably good agreement with literature value for bulk thermal conductivity of single crystal TiO₂ using this B_1 and the boundary size of 1 mm (and neglecting impurity scattering).²¹ Second, boundary scattering is factored in based on the film thickness ($L \sim 200$ nm) using the expression $\Lambda_{\text{boundary}}/\Lambda_{\text{bulk}} = 1 + 3K_n [E_5(K_n^{-1}) - 1/4]$, where K_n is the Knudsen number $K_n = \Lambda_{\text{bulk}}/L$, and E_5 is a numerical function. This is a simplified expression assuming the boundary is diffusive,²⁷ and a good assumption in our work because the specular condition only applies to very low temperature and extremely smooth interface.

Finally, and perhaps most critically, the impurity relaxation time is obtained using $\Lambda_{\text{imp}}^{-1}(\omega) = A\omega^4$ according to the Klemens’ relationship.²⁸ The parameter A can be expressed as

$$A = C\Omega(\Delta M/M)^2/4\pi\nu^3, \quad (1)$$

where C is the doping concentration per unit cell, Ω is the unit cell volume, and $\Delta M/M$ is the relative change in atomic mass per unit cell. Therefore, the stronger phonon-impurity scattering can be explained by a high mass contrast between

Ti and Ta ($Z_{\text{Ti}} = 22$ while $Z_{\text{Ta}} = 72$) compared to other dopants in TiO₂,^{9,29} and it is also theoretically expected to see a monotonic increase in $\Lambda_{\text{imp}}^{-1}$ upon increasing doping density. For instance, the impurity coefficient A is approximately estimated as 6.2×10^{-44} , 4.1×10^{-43} , and 1.0×10^{-42} s³ for 0.3, 2, and 5 at. % Ta:TiO₂, respectively.

Combining all the scattering mechanisms discussed earlier and the phonon dispersion, we computed the lattice thermal conductivity in the cross-plane direction, as denoted by lines in Fig. 4(a). In general, they reasonably agree with the measured thermal conductivity data, supporting the significant reduction in κ upon Ta doping arising from the phonon-impurity scattering. Quantitatively, there is still a noticeable difference between the measured and calculated κ , particularly at lower temperatures. This may imply that the boundary scattering is stronger than the prediction in our films, as we note that the grain sizes are 100–200 nm, which are comparable to the film thickness, shown by TEM investigation. Moreover, the averaged sinusoidal type phonon dispersion we employed might be an over simplification, and the parameters used for the MFP estimation are not directly from thermal characterization (rather from other types of measurements), both of which may cause deviation.

More significantly, our computation based merely on lattice contribution is unable to explain the non-monotonic trend of the experimental κ , found for 5 at. % Ta:TiO₂. That is, it is observed that κ of 5 at. % Ta:TiO₂ is greater than or comparable to that of 2 at. % Ta:TiO₂ at almost all temperatures, despite the expected stronger impurity scattering for the former. For the metallically conductive Ta:TiO₂ with 5 at. % doping, both free electrons and phonons should carry thermal energy while our calculation only reflects the phonon (lattice) contribution. Typically, electronic thermal conductivity can be computed by the Wiedemann-Franz (W-F) law [Fig. 4(b)], and herein we also neglect the weak anisotropy in electrical conductivity of TiO₂.³⁰ Subtracting the W-F law calculated electronic contribution from the measured κ largely eliminate the non-monotonic trend of thermal conductivity with Ta doping, as shown in Fig. 4(c), but still show discrepancy from the computed curves. Moreover, it is well known that more compensating native defects also typically form as more extrinsic dopants are introduced,³¹ so the Ta-doped TiO₂ also possesses such defects like Ti vacancy or Ti³⁺.¹⁴ In other words, the phonon-impurity scattering could be potentially more significant than the initially estimated which accounts only for Ta dopants. Thus, new effects may exist in the case of high Ta doping beyond the simple modification of Λ_{eff} via impurity scattering of phonons. In addition to populating free charge carriers (and strengthening impurity-phonon scattering), dopants can introduce local lattice distortion particularly at high concentrations in spite of the modest difference ($\sim 4\%$) of ionic radii of Ti⁴⁺ and Ta⁵⁺. As we noted earlier, a substantial blueshift (~ 11.3 cm⁻¹) of E_g frequency is observed for the 5 at. % doping in Fig. 1(c), which was recently correlated to a stiffened bulk modulus (B) driven by hydrostatic pressure.^{32,33} In our case, it can be attributed to dopant-induced compressive strain to the host TiO₂ lattice, thereby renormalizing the phonon dispersion resulting in potentially higher group velocity as suggested by $\nu = \sqrt{(B/\rho)}$.

In summary, our work shows that Ta doping in anatase TiO₂ generally results in suppression of κ that could be largely explained by enhanced phonon scattering with impurities. However, beyond this conventional doping effect, for high doping concentrations, we observed that the measured κ no longer shows further reduction, and especially at and above room temperature, κ is close to that of undoped TiO₂. This was attributed to the additional electronic contribution and potentially higher sound velocity by local compressive strain. Our results demonstrate that Ta:TiO₂ is a promising alternative to the conventional TCO with metallic electrical conduction while maintaining reasonably high thermal conductivity. It will eventually lead to understand, design, and optimize the charge and energy transport characteristics of TiO₂, and other TCO candidates, with suitable chemical doping.

See [supplementary material](#) for additional structural and transport data.

This work was supported by NSF Grant No. DMR-1608899. J.W. acknowledges support from the Tsinghua-Berkeley Shenzhen Institute (TBSI). The authors thank Dr. Fan Yang for stimulating discussion and computational assistance. T.V. group acknowledges the Competitive Research Program No. NRF-CRP15-2015-01 and the SrTiO₃ buffered silicon wafer from Professor Darrell Schlom of Cornell University.

¹X. Chen and S. S. Mao, *Chem. Rev.* **107**, 2891 (2007).

²J. Bai and B. Zhou, *Chem. Rev.* **114**, 10131 (2014).

³J. Yan, G. Wu, N. Guan, L. Li, Z. Li, and X. Cao, *Phys. Chem. Chem. Phys.* **15**, 10978 (2013).

⁴K. C. Goddeti, S. M. Kim, Y. K. Lee, S. H. Kim, and J. Y. Park, *Catal. Lett.* **144**, 1411 (2014).

⁵T. Sarkar, K. Gopinadhan, J. Zhou, S. Saha, J. M. D. Coey, Y. P. Feng, Ariando, and T. Venkatesan, *ACS Appl. Mater. Interfaces* **7**, 24616 (2015).

⁶K. M. Yu, M. A. Mayer, D. T. Speaks, H. He, R. Zhao, L. Hsu, S. S. Mao, E. E. Haller, and W. Walukiewicz, *J. Appl. Phys.* **111**, 123505 (2012).

⁷T. Koketsu, J. Ma, B. J. Morgan, M. Body, C. Legein, W. Dachraoui, M. Giannini, A. Demortière, M. Salanne, F. Dardoize, H. Groult, O. J.

Borkiewicz, K. W. Chapman, P. Strasser, and D. Dambournet, *Nat. Mater.* **16**, 1142 (2017).

⁸Y. Furubayashi, T. Hitosugi, Y. Yamamoto, K. Inaba, G. Kinoda, Y. Hirose, T. Shimada, and T. Hasegawa, *Appl. Phys. Lett.* **86**, 252101 (2005).

⁹C. Tasaki, N. Oka, T. Yagi, N. Taketoshi, T. Baba, T. Kamiyama, S.-I. Nakamura, and Y. Shigesato, *Jpn. J. Appl. Phys.* **51**, 035802 (2012).

¹⁰J. Osorio-Guillén, S. Lany, and A. Zunger, *Phys. Rev. Lett.* **100**, 036601 (2008).

¹¹M. Matsubara, R. Saniz, B. Partoens, and D. Lamoën, *Phys. Chem. Chem. Phys.* **19**, 1945 (2017).

¹²H. Anh Huy, B. Aradi, T. Frauenheim, and P. Deák, *J. Appl. Phys.* **112**, 016103 (2012).

¹³P. Mazzolini, P. Gondoni, V. Russo, D. Christina, C. S. Casari, and A. L. Bassi, *J. Phys. Chem. C* **119**, 6988 (2015).

¹⁴A. R. Barman, M. Motapothula, A. Annadi, K. Gopinadhan, Y. L. Zhao, Z. Yong, I. Santoso, Ariando, M. Breesse, A. Rusydi, S. Dhar, and T. Venkatesan, *Appl. Phys. Lett.* **98**, 072111 (2011).

¹⁵T. P. Sarkar, K. Gopinadhan, M. Motapothula, S. Saha, Z. Huang, S. Dhar, A. Patra, W. M. Lu, F. Telesio, I. Pallecchi, Ariando, D. Marré, and T. Venkatesan, *Sci. Rep.* **5**, 13011 (2015).

¹⁶T. Hitosugi, Y. Furubayashi, A. Ueda, K. Itabashi, K. Inaba, Y. Hirose, G. Kinoda, Y. Yamamoto, T. Shimada, and T. Hasegawa, *Jpn. J. Appl. Phys.* **44**, L1063 (2005).

¹⁷D. A. H. Hanaor and C. C. Sorrell, *J. Mater. Sci.* **46**, 855 (2010).

¹⁸D. Cahill, *Rev. Sci. Instrum.* **61**, 802 (1989).

¹⁹C. J. Glassbrenner and G. A. Slack, *Phys. Rev.* **134**, 1058 (1964).

²⁰J. Fang, C. Reitz, T. Brezesinski, E. J. Nemanick, C. B. Kang, S. H. Tolbert, and L. Pilon, *J. Phys. Chem. C* **115**, 14606 (2011).

²¹Y. S. Touloukian, *Thermophysical Properties of Matter* (IFI Plenum, New York-Washington, 1973).

²²F. Yang and C. Dames, *Phys. Rev. B* **87**, 035437 (2013).

²³E. Shojaei and M. R. Mohammadzadeh, *J. Phys.: Condens. Matter* **22**, 015401 (2010).

²⁴D. Morelli, J. Heremans, and G. Slack, *Phys. Rev. B* **66**, 195304 (2002).

²⁵T. Hirata, *Phys. Status Solidi B* **209**, 17 (1998).

²⁶S. J. Smith, R. Stevens, S. Liu, G. Li, A. Navrotsky, J. Boerio-Goates, and B. F. Woodfield, *Am. Miner.* **94**, 236 (2009).

²⁷C. Hua and A. J. Minnich, *J. Appl. Phys.* **117**, 175306 (2015).

²⁸P. G. Klemens, *Proc. Phys. Soc.* **68A**, 1113 (1955).

²⁹S. V. Zaitsev, J. Moon, H. Takagi, and M. Awano, *Adv. Powder Technol.* **11**, 211 (2000).

³⁰M. K. Nowotny, T. Bak, and J. Nowotny, *J. Phys. Chem. B* **110**, 16270 (2006).

³¹W. Walukiewicz, *Physica B* **302-303**, 123 (2001).

³²V. Swamy, A. Kuznetsov, L. S. Dubrovinsky, R. A. Caruso, D. G. Shchukin, and B. C. Muddle, *Phys. Rev. B* **71**, 735 (2005).

³³X. J. Liu, L. K. Pan, Z. Sun, Y. M. Chen, X. X. Yang, L. W. Yang, Z. F. Zhou, and C. Q. Sun, *J. Appl. Phys.* **110**, 044322 (2011).

Supplementary Material for

Compensated thermal conductivity of metallically conductive Ta-doped TiO₂

Joonki Suh,^{1,a),b)} Tarapada Sarkar,^{2,3} Hwan Sung Choe,¹ Joonsuk Park,⁴ T. Venkatesan,^{2,3,5,6,7}
Junqiao Wu^{1,8,b)}

¹*Department of Materials Science and Engineering, and Tsinghua-Berkeley Shenzhen Institute, University of California, Berkeley, California 94720, USA*

²*Department of Physics, National University of Singapore, Singapore 117542*

³*NUSNNI-NanoCore, National University of Singapore, Singapore 117576*

⁴*Department of Materials Science and Engineering, Stanford University, Stanford, California 94305, USA*

⁵*Department of Electrical Engineering, National University of Singapore, Singapore 117583*

⁶*Department of Integrative Science and Engineering, National University of Singapore, Singapore, 117456*

⁷*Department of Materials Science and Engineering, National University of Singapore, Singapore 117575*

⁸*Materials Sciences Division, Lawrence Berkeley National Laboratory, Berkeley, California 94720, USA*

^{a)}Present address: Department of Chemistry, University of Chicago, Chicago, Illinois 60637, USA

^{b)}Author to whom correspondence should be addressed. Electronic addresses: wuj@berkeley.edu and joonki@uchicago.edu

Out high-resolution transmission electron microscopy (HRTEM) analysis verifies the preferential epitaxial growth relation, anatase-TiO₂ (001) || SrTiO₃ (100) as shown in Figure S1. More specifically, FFT pattern analysis identifies (020) spots in STO (ICDD 05-0634) and anatase TiO₂ (ICDD 21-1272), confirming lattice parameters $a_{\text{STO}} = 0.39$ nm, $a_{\text{TiO}_2} = 0.378$ and $c_{\text{TiO}_2} = 0.951$ nm, respectively. This epitaxial relationship is relatively well established for anatase TiO₂ thin films grown by pulsed laser deposition¹ or molecular beam epitaxy,² and also demonstrated with other perovskite overlayers.^{3,4}

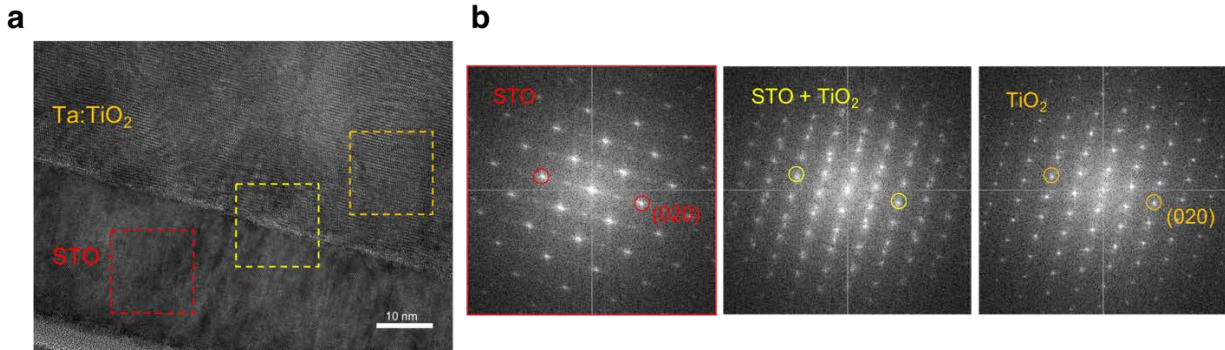


FIG. S1. (a) Cross-sectional high-resolution transmission electron microscopy (HRTEM) image at the interface of SrTiO₃ (STO) and Ta-doped TiO₂ (Ta:TiO₂) layers. (b) Corresponding fast Fourier transform (FFT) patterns acquired from STO, STO/Ta:TiO₂ interface, and TiO₂ regions.

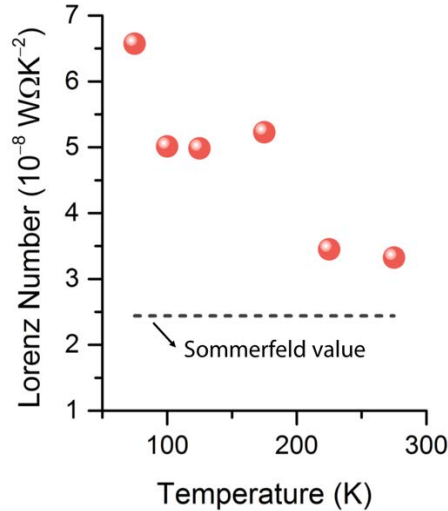


FIG. S2. For the measured κ_{total} of the 5 at.% Ta-doped TiO₂, if κ_{lattice} is set to be equal to the alloy-scattering model predicted value, the expected Lorenz number needs to be unusually high. As the Wiedemann-Franz law is not expected to be violated in this system, this contradiction indicates the existence of additional effects beyond the conventional contributions of alloy scattering and charge carriers to κ_{total} .

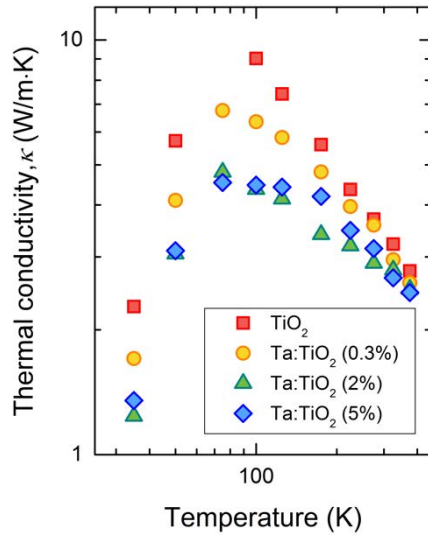


FIG. S3. The measured thermal conductivity data in log-log plot to show more details of the low-value portion.

Supplementary References

1. T. Hitosugi *et al.* Ta-doped anatase TiO₂ epitaxial film as transparent conducting oxide. *Jpn. J. Appl. Phys.* **44**, L1064 (2005).
2. X. Weng *et al.* Structural characterization of TiO₂ films grown on LaAlO₃ and SrTiO₃ substrates using reactive molecular beam epitaxy. *J. Cryst. Growth* **310**, 545 (2008).
3. M. Murakami, Anatase TiO₂ thin films grown on lattice-matched LaAlO₃ substrate by laser molecular-beam epitaxy. *Appl. Phys. Lett.* **78**, 2664 (2001).
4. T. Tachikawa *et al.* Metal-to-insulator transition in anatase TiO₂ thin films induced by growth rate modulation. *Appl. Phys. Lett.* **101**, 022104 (2012).